

# Efficient Unsupervised Domain Adaptation Regression for Spatial-Temporal Air Quality Sensor Fusion

Keivan Faghah Niresi<sup>a</sup>, Ismail Nejjar<sup>a</sup>, Olga Fink<sup>a</sup>

<sup>a</sup>*Intelligent Maintenance and Operations Systems (IMOS) Lab, EPFL, Switzerland,*

---

## Abstract

The deployment of affordable Internet of Things (IoT) sensors for air pollution monitoring has increased in recent years due to their scalability and cost-effectiveness. However, accurately calibrating these sensors in uncontrolled environments remains a significant challenge. While expensive reference sensors can provide accurate ground truth data, they are often deployed on a limited scale due to high costs, leading to a scarcity of labeled data. In diverse urban environments, data distributions constantly shift due to varying factors such as traffic patterns, industrial activities, and weather conditions, which impact sensor readings. Consequently, traditional machine learning models – despite their increasing deployment for environmental sensor calibration – often struggle to provide reliable pollutant measurements across different locations due to domain shifts. To address these challenges, we propose a novel unsupervised domain adaptation (UDA) method specifically tailored for regression tasks on graph-structured data. Our approach leverages Graph Neural Networks (GNNs) to model the relationships between sensors. To effectively capture critical spatial-temporal interactions, we incorporate spatial-temporal graph neural networks (STGNNs), which extend GNNs by incorporating temporal dynamics. To handle the resulting larger embeddings, we propose a domain adaptation method using a closed-form solution inspired by the Tikhonov-regularized least-squares problem. This method leverages Cholesky decomposition and power iteration to align the subspaces between source and target domains. By aligning these subspaces, our approach allows low-cost IoT sensors to learn calibration parameters from expensive reference sensors. This facilitates reliable pollutant measurements in new locations without the need for additional costly equipment. Experimental evaluations on real-world datasets show that our method achieves competitive performance while significantly reducing training time, making

it practical for large-scale air pollution monitoring in urban environments.

*Keywords:* Unsupervised domain adaptation, Graph neural networks, Multisensor fusion, Internet of Things, Air quality, Smart cities

---

## 1. Introduction

The increase in air pollution, driven by growing urban population densities, escalating vehicular traffic, and expanding industrial emissions, poses a significant threat to both public and environmental health. Various pollutants such as carbon monoxide (CO), nitrogen dioxide (NO<sub>2</sub>), and tropospheric ozone (O<sub>3</sub>) are particularly hazardous [1]. Therefore, it is essential to establish reliable air quality monitoring systems that focus on different contaminants to track environmental progress, provide warnings to inhabitants, and support informed decision-making for public health and safety. Such monitoring contributes to the overall objectives of developing environmentally friendly and livable urban environments, characteristics of smart and sustainable cities [2]. These systems are also essential for safeguarding public health and contributing to the effective management of pollutants.

The advent of the Internet of Things (IoT) has played a crucial role in advancing smart and sustainable urban environments [3]. IoT-based technologies have made it possible to collect real-time data from various sensors installed and distributed across different locations [4]. However, despite these advancements, concerns persist regarding the accuracy of low-cost sensors integrated into IoT-based solutions [5, 6]. Manufacturers typically do not calibrate environmental sensors, and if they do, the calibration is not performed under the actual environmental conditions where the sensors will operate. This can negatively impact the performance of the sensor network [7]. To address this challenge, many air quality monitoring platforms incorporate inexpensive temperature and humidity sensors alongside gas sensors to enable reliable calibration [8]. Nevertheless, implementing low-cost sensor networks presents specific challenges such as sensor drift, interference from environmental factors, and discrepancies in sensor calibration, which can lead to inaccurate data readings. These sensor networks often struggle with limited sensitivity, making it difficult to measure specific contaminants precisely. Moreover, sensor network maintenance and data validation can be complex, as individual sensor reliability may vary, affecting overall data quality and consistency [9]. These challenges can significantly hinder the utilization of

such sensor networks in regulatory pollutant measurements, necessitating the use of expensive and high-precision measuring devices as references for calibration. One potential strategy to enhance the reliability of low-cost sensor networks involves incorporating hardware redundancy across the sensor network. Additionally, employing multisensor fusion methods could enable the utilization of all low-cost sensors to achieve highly reliable measurements for various pollutants [10].

Traditional machine learning algorithms such as support vector regression (SVR), random forest (RF), and k-nearest neighbors (KNN) have been shown to be feasible options for multisensor fusion and calibration in IoT-based air pollution monitoring platforms [7]. Despite their fairly good performance, these traditional machine learning models still face challenges in achieving reliable estimation of air pollutants, limiting their deployment reliability. One limitation of these models is their dependency on extensive feature engineering before data input. For instance, air quality sensor networks often experience multicollinearity, where multiple sensors provide highly correlated information. This redundancy not only diminishes model performance but also leads to inefficient training processes. Effective feature engineering in such contexts requires substantial domain knowledge and can be highly specialized, presenting challenges in developing reliable machine learning models. Moreover, these models typically fail to account for the spatial and temporal interactions among sensor measurements that are particularly relevant in air quality sensor networks. Although temporal pattern-based denoising can improve performance as a post-processing step following fusion and calibration, as indicated in [11], there remains a critical need for a model that can jointly capture both spatial and temporal features in a comprehensive, end-to-end approach.

Spatial-temporal graph neural networks (STGNNs) have emerged as powerful tools in various applications due to their ability to capture complex spatial-temporal relationships within data [12]. This versatility has been demonstrated in different fields such as traffic data analysis [13, 14, 15], industrial IoT [16, 17], and evolving social networks [18]. Leveraging their capability to capture spatial-temporal interactions among sensor measurements, a recent study applied STGNNs for multisensor fusion and calibration in IoT air pollution monitoring platforms [19]. This study showed that this architecture can achieve promising results compared to other data-driven methods that did not leverage the graph structure of air quality sensor networks.

STGNNs typically perform well when the testing data distribution aligns

with the training data distribution. However, in real-world scenarios, especially in diverse urban environments, data distributions are prone to change over time. This shift can result in performance degradation. This occurs because most current data-driven models assume that the statistical properties of data remain the same [20]. In the context of air quality monitoring, geographical variations due to factors such as weather conditions, pollution sources, and urban planning can cause significant differences in data distributions. Consequently, models trained in one location may not perform when applied in another. A straightforward but expensive solution would be to collect new labeled data at each specific measurement location and train a separate model for each deployment site. This method requires high-precision instruments at each site for accurate calibration, which can be prohibitively costly. Therefore, an alternative approach is needed that uses available labeled data from a specific location and adapts the model to different locations without relying on high-precision sensors at each site.

To address this challenge, unsupervised domain adaptation (UDA) shows promise in transferring knowledge from a labeled source domain to a related but unlabeled target domain [21]. UDA would allow for the utilization of only a single high-precision sensor in the source domain, eliminating the need for labeled data in the target domain. As a result, the need to deploy and manage multiple high-precision sensors across different environments is eliminated, reducing overall costs.

Various UDA approaches have been applied to time series data to minimize discrepancies across domains by using domain-invariant temporal features extracted through convolutional neural networks (CNNs) and long short-term memory (LSTM) [22, 23]. However, sensor networks, exhibit spatial-temporal interdependencies among sensors that must be considered for effective fusion and adaptability. Therefore, when applying UDA to spatial-temporal data, it is crucial to address both temporal and spatial interactions. For graph-structured data, minimizing the maximum mean discrepancy (MMD) loss [24] has been shown to generate transferable node embeddings suitable for cross-network learning tasks [25]. Additionally, domain adversarial learning strategies [26, 27, 28] combined with graph convolutional networks (GCNs) as feature extractors have demonstrated improved adaptability across different domains by generating domain-invariant node representations. However, UDA methods for graph-structured data are predominantly designed for classification tasks and often overlook the temporal dependencies of sensor (node) values. This limitation reduces their effec-

tiveness in multisensor fusion and calibration tasks, which require models to predict continuous values [29, 30].

Recently, novel UDA methods have emerged with a focus on regression tasks. Notably, Representation Subspace Distance for Domain Adaptation Regression (RSD) [29] aims to align orthogonal bases while preserving the feature scale. The RSD-based approach has shown improved results, highlighting the need for UDA methods specifically designed for regression tasks.

Alternatively, the DARE-GRAM [30] method approaches UDA for regression from a regressor’s perspective. Motivated by the closed-form least square solution, this method proposes aligning the pseudo-inverse of the Gram matrix instead of directly aligning the features. DARE-GRAM, which focuses on scale and angle alignment based on the Gram matrix, results in better-calibrated features for the regressor and exhibits less sensitivity to batch size compared to RSD.

Although these two subspace-based approaches [29, 30] provide state-of-the-art results for UDA in regression tasks, each training iteration requires computationally intensive singular value decomposition (SVD), which can be computationally too expensive for large-scale sensor networks.

To address existing limitations, this study proposes a novel UDA method for regression tasks that delivers state-of-the-art results while being faster and more scalable. Specifically, we introduce a Tikhonov-regularized least squares-based unsupervised deep domain adaptation (TikUDA) method. This approach aligns the inverse of the Gram matrix of the features, perturbed by a scaled identity matrix known as the Tikhonov matrix. This perturbation reduces the condition number of the Gram matrix. The full-rank properties of the Tikhonov matrix allow us to use faster decomposition methods rather than relying on singular value decomposition, ensuring stable training and reducing training time. This is particularly relevant for graph neural networks (GNNs) as the number of nodes (sensors) increases. As the network expands, more sensors are aggregated in the embedding space, thus increasing its dimensionality.

Building on this foundation, the primary goal of this paper is to develop a robust methodology for estimating pollutant levels using low-cost sensors in various urban environments. Our approach leverages the proposed TikUDA method to bridge the gap between two domains: training on labeled data from low-cost sensors calibrated with a high-precision sensor in one location (the source domain) and transferring that knowledge to a different location (target domain) using unlabeled data from low-cost sensors.

To capture both spatial and temporal dependencies in sensor measurements, we propose using spatial-temporal graph neural networks (STGNNs) within IoT air quality sensor networks. The model first encodes input data into a hidden space with a linear encoder. Temporal dependencies are then extracted using a Gated Recurrent Unit (GRU), followed by spatial pattern extraction using a Graph Attention Network (GAT). To ensure the model generalizes well to the target location, we apply our TikUDA method to align the feature representations from both the source and target domains.

Our experimental results, based on real-world datasets, demonstrate the effectiveness of this approach in estimating air pollutants and improving generalization to new target locations using low-cost sensors. This significantly reduces the dependency on numerous high-precision reference sensors, thus lowering both cost and system complexity. To the best of our knowledge, this study is the first to apply UDA in the context of multisensor fusion and calibration for IoT air quality sensor networks, providing a scalable and efficient solution for improving air quality monitoring in smart and sustainable cities.

The key contributions of this article are as follows:

1. We propose a novel UDA method tailored for spatial-temporal regression tasks that provides state-of-the-art results with improved scalability and faster execution.
2. We proposed a new UDA method for regression tasks by utilizing the well-known closed-form solutions from Tikhonov regularization, commonly used in linear inverse problems.
3. We integrate this UDA method with STGNNs, effectively capturing both temporal dynamics and graph-structured data, demonstrating the strength of this combined approach.
4. We evaluate the proposed method on real-world IoT air quality sensor network datasets, showcasing its practical applicability and superior performance in real-world applications.

The remainder of the paper is organized as follows: Section 2 provides an in-depth introduction to the relevant background in multisensor fusion and unsupervised domain adaptation for regression tasks. In Section 3, we present the proposed spatial-temporal feature extractor along with our proposed TikUDA method for unsupervised domain adaptation. Sections 4 and 5 detail the experimental setup and results, illustrating the efficacy of our

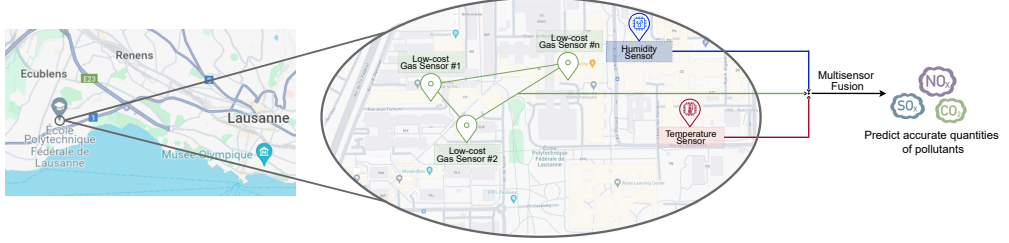


Figure 1: Diagram for Multisensor Fusion in IoT Air Quality Monitoring.

approach compared to various baseline and state-of-the-art methods. Finally, Section 6 summarizes the findings and suggests possible directions for future research.

## 2. Problem Definition

### 2.1. Multisensor Fusion and Calibration

Multisensor data fusion and calibration involve the integration of data from multiple sensors, denoted as  $\{s_1, \dots, s_n\}$ , within an IoT air quality sensor network. These sensors measure various environmental parameters such as pollutants, humidity, and temperature. The goal is to produce highly reliable estimates of pollutant levels, including ozone and nitrogen dioxide values, by aggregating data from a set of sensors that include not only unreliable gas measurement sensors but also measure temperature and humidity as illustrated in Figure 1.

Given the spatial-temporal characteristics of urban data, several studies have integrated GNNs with different learning strategies to capture dynamics in both space and time [31]. Building on this research, we propose using a Spatial-Temporal Graph Neural Network (STGNN) model for IoT air quality sensor prediction. STGNNs are designed to capture both spatial and temporal relationships within data by leveraging the spatial interactions among sensors and the temporal patterns in their measurements.

However, relying solely on direct predictions from low-cost IoT air quality sensors is insufficient for training an accurate multisensor fusion model in new locations. In this paper, we propose leveraging labeled data from low-cost IoT air quality sensor networks deployed in a specific urban area. These data are strategically collected from sites near high-precision sensors used by governmental agencies, serving as ground truth labels in the source

domain. Additionally, we use unlabeled data obtained from low-cost IoT air quality sensors in new locations (target domain), which are sufficiently distant from the source location to experience a domain shift. To counteract the performance degradation caused by this shift and to deploy the model in the new location without high-precision sensors, we employ unsupervised domain adaptation (UDA). This approach mitigates the impact of domain shift and ensures accurate predictions of pollutant levels. We assume that the IoT air quality sensor networks in both locations maintain an identical number of sensors.

## 2.2. Unsupervised Domain Adaptation

Unsupervised Domain Adaptation (UDA) aims to overcome the distribution shift between a labeled source domain and an unlabeled target domain. Especially, we aim to learn a model  $f_\theta$  that generalizes well to the target domain. In other words, we aim to minimize the expected error on the target data:

$$\arg \min_{\theta} \mathbb{E}\{\|f_\theta(\mathbf{x}^{tgt}) - y^{tgt}\|_2^2\}, \quad (1)$$

where  $\mathbf{y}^{tgt}$  denotes the ground truth label for the target input feature  $\mathbf{x}^{tgt}$  and is not available during training.

Different methods aim to minimize the learned feature discrepancy between the source and target domain. Formally, the model  $f_\theta(\cdot)$ , can be represented by a feature encoder  $h_\theta(\cdot)$  and a regressor  $g_\theta(\cdot)$  that maps the learned feature representation for the input data  $\mathbf{z} = h_\theta(\mathbf{x})$  to the predicted pollutant level  $\hat{y} = g_\theta(\mathbf{z})$ . During training, the feature matrix for a batch size  $b$  can be expressed as  $\mathbf{Z} = [\mathbf{z}_1, \dots, \mathbf{z}_b]$ , where  $\mathbf{Z} \in \mathbb{R}^{b \times p}$  with  $p$  the feature dimension.

DARE-GRAM [30], motivates aligning the inverse Gram matrix  $(\mathbf{Z}^\top \mathbf{Z})^{-1}$  from the well-known closed-form solution of the ordinary least-squares (OLS) to ensure a feature representation that is similar from a regressor perspective. However, in deep learning models, the batch size is often smaller than the feature dimension, i.e.,  $b < p$ , resulting in a feature matrix  $\mathbf{Z} \in \mathbb{R}^{b \times p}$ . Consequently, the Gram matrix  $(\mathbf{Z}^\top \mathbf{Z} \in \mathbb{R}^{p \times p})$  may have a rank  $r \leq b$ , leading to an ill-conditioned matrix that is not invertible. To address this, DARE-GRAM proposed using the Moore-Penrose pseudo-inverse, which generalizes the concept of matrix inversion for matrices that may not be invertible. Additionally, a threshold is applied to singular values to focus on a selected

subspace of the inverse Gram matrix. However, the practical implementation of such an algorithm relies on two singular value decompositions, which is computationally expensive. In this paper, we propose an improved method that is less computationally expensive.

### 3. Methodology

In this work, we propose a Tikhonov-regularized least squares-based unsupervised domain adaptation (TikUDA) method. This method improves over previous methods, as detailed in Section 3.1. Furthermore, we introduce a Spatial-Temporal Graph Neural Network (STGNN) designed to effectively capture both spatial and temporal interactions in multisensor fusion tasks. This model leverages the spatial correlations between different sensor nodes and temporal dependencies within their measurements, providing a promising framework for integrating and analyzing information from multiple sensors over time, as detailed in Section 3.2. In Section 3.3, we provide a comprehensive overview and summary of the overall framework.

#### 3.1. *TikUDA*

To alleviate the ill-conditioned problem of the Gram matrix, we propose using the closed-form solution of Ridge regression – a specific case of Tikhonov-regularized least-squares – instead of using the closed-form solution of OLS. Specifically, we apply the Tikhonov matrix  $\mathbf{Z}^T \mathbf{Z} + \alpha \mathbf{I}$ , which ensures the Gram matrix is fully ranked by adding the identity matrix. This addition guarantees the smallest eigenvalue is never zero but it depends on  $\alpha$ . This eliminates the need to compute the SVD to threshold degenerate spaces (small eigenvalues) and allows for direct inverse matrix decomposition. Following DARE-GRAM methodology [30], we propose aligning the subspaces of the source and target domains using the angle between the columns of the inverse Tikhonov matrix, which are ordered based on the importance of their eigenvalue. To ensure consistent scaling between the source and target feature representations, we align their eigenvalues, addressing the scale sensitivity in regression models as highlighted in [29].

**Angle Alignment:** The inverse Tikhonov matrices for the source and target domains are represented as:

$$\mathbf{G}_s^{-1} = (\mathbf{Z}_{\text{src}}^T \mathbf{Z}_{\text{src}} + \alpha \mathbf{I})^{-1} \quad (2)$$

$$\mathbf{G}_t^{-1} = (\mathbf{Z}_{\text{tgt}}^T \mathbf{Z}_{\text{tgt}} + \alpha \mathbf{I})^{-1} \quad (3)$$

respectively. Since the Tikhonov matrix is symmetric and positive definite, its inverse can be computed more efficiently using methods such as Cholesky decomposition [32]. This approach reduces the computational complexity of our proposed algorithm, making it more practical for larger matrices.

Previous methods utilized cosine similarity to measure the angle difference between the source and target using the column space of  $\mathbf{G}_s^{-1}$  and  $\mathbf{G}_t^{-1}$ , and is defined as follows:

$$\cos(\phi_{(i)}^{S \leftrightarrow T}) = \frac{\mathbf{G}_{s,i}^{-1} \cdot \mathbf{G}_{t,i}^{-1}}{\|\mathbf{G}_{s,i}^{-1}\| \cdot \|\mathbf{G}_{t,i}^{-1}\|}, \quad (4)$$

where  $i \in [1, p]$  represents the  $i$ -th column (out of a total of  $p$  columns) of the inverse Tikhonov matrix. A major drawback of using cosine similarity is that when the angle between two vectors is small, the cosine value approaches 1, leading to a loss of precision and sensitivity in distinguishing between vectors that are nearly parallel. This can pose challenges in applications where subtle differences are crucial, making it difficult to effectively compare them. To address this issue, we introduce the haversine similarity (HS), defined as follows:

$$\text{HS}(\phi_{(i)}^{S \leftrightarrow T}) = 1 - \sqrt{\frac{1 - \cos(\phi_{(i)}^{S \leftrightarrow T})}{2}}. \quad (5)$$

The proposed haversine similarity metric effectively penalizes differences in angles, especially for small ones. We argue that the haversine similarity is more suitable for subspace alignment, as it enforces closer angular alignments between the columns of the inverse Tikhonov matrices of the source and target domains. Figure 2 illustrates the differences between these two metrics for clearer understanding.

The HS values between the subspace spans of the source and target features are assigned to  $\mathbf{m} = [\text{HS}(\phi_{(1)}^{S \leftrightarrow T}), \dots, \text{HS}(\phi_{(p)}^{S \leftrightarrow T})]$ . Thus, the loss function to align the bases from the inverse Tikhonov matrix can be expressed as:

$$L_{\text{angle}} = \|\mathbf{1} - \mathbf{m}\|_1 \quad (6)$$

where  $\mathbf{1}$  is a vector of ones with shape  $p$ . Minimizing this loss function (6) maximizes the haversine similarity between the representation subspaces of the source and target by reducing the angle between the bases of both domains.

**Scale Alignment :** In addition to angle alignment, which was discussed in the previous subsection, maintaining feature scale consistency across the

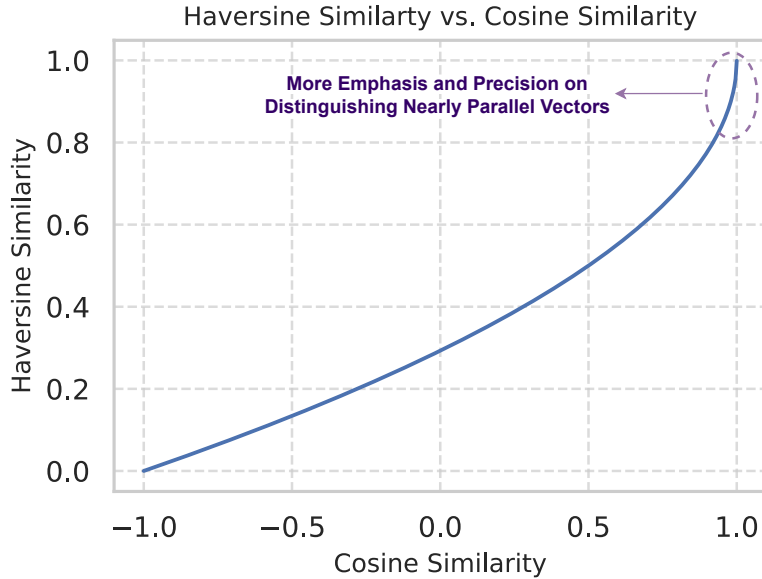


Figure 2: Comparison of cosine similarity and the haversine similarity function.

source and target domains is essential for effective UDA in regression tasks. We find that in regression scenarios, the largest principal eigenvalue ( $\lambda_{\max}$ ) has the most significant impact on feature scaling. Hence, in contrast to the DARE-GRAM [30], which selects k-principal eigenvalues for scaling through singular value decomposition (SVD), we only consider the largest eigenvalue of the feature matrix. Our approach avoids the computationally intensive SVD procedure typically used to identify the k-principal eigenvalues. Instead, we can efficiently compute the largest eigenvalue using methods such as the Lanczos algorithm and power methods [33]. Thus, the regularization of the scale alignment between the features of the source and target is achieved by minimizing the discrepancy between their first principal eigenvalue as:

$$L_{\text{scale}} = (\lambda_{\max}^{\text{src}} - \lambda_{\max}^{\text{tgt}})^2. \quad (7)$$

### 3.2. Spatial-Temporal Feature Extractor

To effectively capture both spatial and temporal features, current STGNNs utilize two types of architectures: time-then-space (factorized) and time-and-space (coupled) [34]. In time-then-space designs, temporal processing occurs before spatial processing. Both theoretical and empirical evidence suggest that time-then-space architectures, when using GNNs components

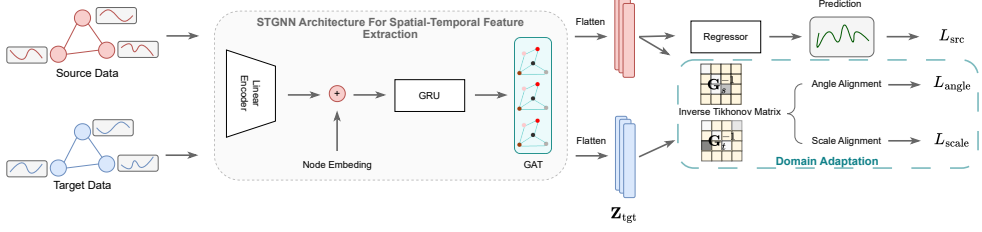


Figure 3: An overview of the proposed approach for domain adaptive regression problems on spatial-temporal graph data

constrained to the 1-Weisfeiler-Lehman (1-WL) power [35], provide a performance advantage compared to time-and-space architectures that utilize the same 1-WL GNN components [36]. Given these advantages, we opt for the time-then-space architecture for multisensor fusion to achieve more accurate predictions.

**Temporal Module of Feature Extractor :** Temporal dependencies, also known as temporal patterns, can be effectively represented in both the time domain and the frequency domain [34]. To address these dependencies, we incorporate temporal modules before spatial modules, facilitating the modeling of complex spatial-temporal patterns. Our approach adopts recurrence-based methodologies, specifically leveraging the Gated Recurrent Unit (GRU), to capture and interpret the underlying temporal patterns inherent in the time series data by:

$$\mathbf{r}_t = \sigma(\mathbf{W}_r \mathbf{x}_t + \mathbf{U}_r \mathbf{h}_{t-1} + \mathbf{b}_r) \quad (8)$$

$$\mathbf{z}_t = \sigma(\mathbf{W}_z \mathbf{x}_t + \mathbf{U}_z \mathbf{h}_{t-1} + \mathbf{b}_z) \quad (9)$$

$$\hat{\mathbf{h}}_t = \tanh(\mathbf{W}_h \mathbf{x}_t + \mathbf{U}_h (\mathbf{r}_t \odot \mathbf{h}_{t-1}) + \mathbf{b}_h) \quad (10)$$

$$\mathbf{h}_t = (1 - \mathbf{z}_t) \odot \mathbf{h}_{t-1} + \mathbf{z}_t \odot \hat{\mathbf{h}}_t \quad (11)$$

In this formula,  $\odot$  represents the Hadamard product operator,  $\mathbf{x}_t$  is the input vector,  $\mathbf{r}_t$  represents the reset gate vector, which controls how much of the previous state should be ignored,  $\mathbf{z}_t$  represents the update gate, which determines how much of the previous state should be passed along,  $\hat{\mathbf{h}}_t$  represents the new gate, which computes the new candidate values for the memory cell, and  $\mathbf{h}$  is the output vector.

**Spatial Module of Feature Extractor :** We employ a series of message-

passing operators to capture the spatial relationships among sensor measurements, iteratively updating representations at each layer [37]. The process of these iterative updates can be described as follows:

$$\mathbf{m}_{\mathcal{N}}^{(k)}(u) = \text{AGG} \left\{ (\text{MSG}^k(\mathbf{h}_u^{(k)}, \mathbf{h}_v^{(k)}), \forall v \in \mathcal{N}(u)) \right\}, \quad (12)$$

$$\mathbf{h}_u^{(k+1)} = \text{UPDATE}^{(k)} \left( \mathbf{h}_u^{(k)}, \mathbf{m}_{\mathcal{N}}^{(k)}(u) \right), \quad (13)$$

where  $\mathbf{h}_u^{(k)}$  denotes the embedding of node  $u$  at the  $k$ -th layer. The functions responsible for updating (UPDATE) and messaging (MSG) can be realized through any differentiable function, such as a multilayer perceptron (MLP). The aggregation operation (AGG) represents a permutation-invariant aggregation operator. Here,  $\mathcal{N}(u)$  denotes the set of neighboring nodes of node  $u$ . To improve the aggregation layer in GNNs, one can assign attention weights to each neighbor, regulating their influence during the aggregation process. In Graph Attention Networks (GAT) [38], attention weights are used to compute a weighted sum of neighboring node embeddings as follows:

$$\mathbf{m}_{\mathcal{N}(u)} = \sum_{v \in \mathcal{N}(u)} \alpha_{u,v} \mathbf{h}_v \quad (14)$$

where  $\alpha_{u,v}$  represents the attention weight assigned to neighbor  $v \in \mathcal{N}(u)$  when aggregating information at node  $u$ . It can be defined as follows:

$$\alpha_{u,v} = \frac{\exp(\text{LeakyReLU}(\mathbf{a}^\top \cdot [\mathbf{W}\mathbf{h}_u || \mathbf{W}\mathbf{h}_v]))}{\sum_{v' \in \mathcal{N}(u)} \exp(\text{LeakyReLU}(\mathbf{a}^\top \cdot [\mathbf{W}\mathbf{h}_u || \mathbf{W}\mathbf{h}_{v'}]))} \quad (15)$$

where  $\mathbf{a}$  represents a trainable attention vector,  $\mathbf{W}$  is a trainable matrix, and  $||$  denotes the concatenation operation. For brevity, the  $k$ -th GAT layer can be represented compactly as:

$$\mathbf{H}^{(k)} = \text{GAT}^{(k)}(\mathbf{H}^{(k-1)}, \mathbf{A}), \quad (16)$$

where  $\mathbf{A}$  is the adjacency matrix that represents the connections between nodes in the graph.

### 3.3. Overall Framework and Summary

The feature extraction architecture implemented in this study captures both temporal and spatial dependencies within the data, following a time-then-space approach as illustrated in Figure 3. Initially, the input data undergoes an encoding process that projects the input features into a hidden

space using a linear encoder. In IoT air quality sensor networks, sensors can display diverse characteristics that are interconnected in complex ways. For instance, in sensor networks including temperature, humidity, and low-cost gas sensors, temperature sensors may exhibit correlated (either similar or opposite) patterns of behavior, as might the humidity sensors. To accurately represent the different conditions affecting each sensor’s behavior, we assign an embedding vector to each sensor to capture its unique characteristics. These embeddings are initially set to random values and then trained alongside the model, allowing them to adapt based on the data and interdependencies within the sensor network.

Next, the data undergoes a temporal processing step using GRU to identify and extract temporal patterns. This is followed by a spatial processing step employing a GAT, leveraging a fully connected graph due to the absence of a predefined graph structure. The extracted features are then inputted into a regressor to predict the quantities of pollutants.

The training objective is to minimize both the prediction error on the source domain and the alignment of features between the source and target domains. The total loss function can be expressed as:

$$L_{\text{total}} = L_{\text{src}} + \gamma_{\text{angle}} L_{\text{angle}} + \gamma_{\text{scale}} L_{\text{scale}}, \quad (17)$$

The loss term  $L_{\text{src}}$  represents the supervised loss (mean squared error) on the source domain, comparing the prediction with the ground truth. The terms  $L_{\text{angle}}$  and  $L_{\text{scale}}$  account for the angle and scale alignment with respect to the inverse Tikhonov matrix. The hyperparameters  $\gamma_{\text{angle}}$  and  $\gamma_{\text{scale}}$  control the influence of angle and scale alignment on the total loss. Finally, for a detailed representation of the domain adaptation part from source to target, Figure 4 illustrates the flowchart of TikUDA. In summary, TikUDA is designed to align the inverse of the Gram matrix of features, which is perturbed by a scaled identity matrix referred to as the Tikhonov matrix. This perturbation ensures that the Gram matrix becomes full rank and invertible. A key aspect of the method is that the Tikhonov matrix is both symmetric and positive definite, which allows for the use of Cholesky decomposition—a more computationally efficient approach to matrix inversion compared to SVD, particularly for large matrices. Cholesky decomposition, specifically suited for symmetric and positive definite matrices, enhances numerical stability while maintaining the structural properties of the Tikhonov matrix. Additionally, TikUDA introduces novel similarity metrics (Haversine

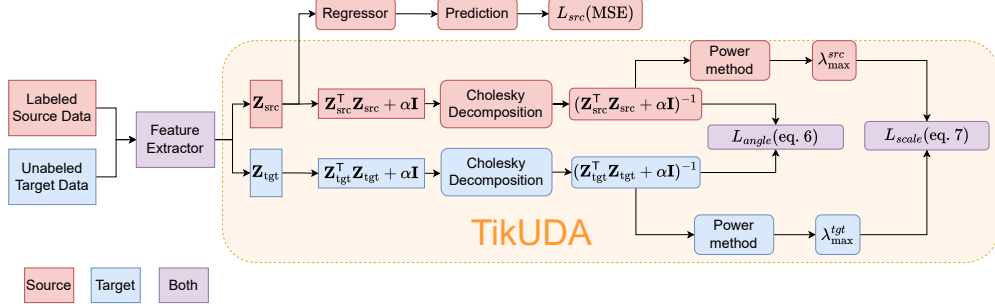


Figure 4: Diagram of the Proposed TikUDA

similarity) as regularization terms to improve subspaces' alignment between the source and target feature domains. Moreover, TikUDA focuses on scale alignment between source and target domains by aligning the largest principal eigenvalues of the inverse Tikhonov matrices, as the largest eigenvalue demonstrates the greatest influence on feature scaling. Instead of computing all eigenvalues through full SVD and then selecting the largest, TikUDA uses the power method to directly approximate the largest eigenvalue. This reduces the computational cost compared to full SVD, making the approach more efficient while ensuring effective alignment between source and target domains.

## 4. Experimental Setup

### 4.1. Case Study

We assess our proposed method using two publicly available real-world datasets from IoT air quality sensor networks [39, 40]. The networks are located in Monte Cucco, an urban area in the province of Piacenza (Italy), designated as R-N69, and in Osio Sotto in Bergamo (Italy), designated as R-N212. Both networks were installed near reference stations operated by governmental agencies using high-precision instrumentation, providing a reliable ground truth for evaluation. Each network is equipped with a low-cost O<sub>3</sub> sensor, NO<sub>2</sub> sensor, temperature sensor, and relative humidity sensor. A detailed summary of the datasets is provided in Table 1 [11]. These two networks are separated by a considerable distance, leading to a distribution shift in sensor measurements, as illustrated in Figure 5. We evaluate the two datasets in both configurations: first using one dataset as the source and the other as the target, then reversing their roles. In Figure 6, we illustrate

the effect of distribution shift on model performance in our experimental setup. As depicted, when the model is trained and deployed at the same measurement location, the performance remains competitive due to the fact that the distribution of the features remains constant. However, when the model is deployed at a different measurement location, a significant drop in performance is observed. This drop is attributed to the distribution shift between the source and target locations. We imitate a practical scenario where reliable ground truth measurements are not available at the target location. The task involves training a model on one labeled dataset (source) to predict reliable  $O_3$  and  $NO_2$  values at the target location.

Table 1: Summary of the Air Quality Datasets Used in the Study,

Dataset Name	Sensor Arrays (outputs are <b>bolded</b> )	Sensor Type	Location	Samples	Timeline
R-69	<b><math>O_3</math>, <math>NO_2</math>, <math>O_3</math> (low-cost), <math>NO_2</math> (low-cost), Temperature, Relative Humidity</b>	OX-B431/NO2-B43F DHT1-Grove	Monte Cucco	1 per hour	21/06/2018 - 25/09/2018
R-212	<b><math>O_3</math>, <math>NO_2</math>, <math>O_3</math> (low-cost), <math>NO_2</math> (low-cost), Temperature, Relative Humidity</b>	OX-B431/NO2-B43F DHT1-Grove	Osio Sotto	1 per hour	27/06/2018 - 24/09/2018

#### 4.2. Data Preprocessing

To prepare the data, each sensor measurement was scaled to a range of  $[0, 1]$  using a min-max normalization approach. The scaling parameters were fitted on the source domain data for each adaptation task and then applied to the target domain data. All data from both domains were used in training for each adaptation task, and no train-test splitting was used. Sensor measurements were segmented into samples using a sliding window approach with a window size of 16 and a step size of 1.

#### 4.3. Evaluation Metrics

We evaluate and compare the performance of the proposed framework using two commonly used regression evaluation metrics: root-mean-square error (RMSE) and mean absolute error (MAE).

$$RMSE = \sqrt{\frac{1}{n} \sum_{i=1}^n (y_i - \hat{y}_i)^2}, \quad (18)$$

$$MAE = \frac{1}{n} \sum_{i=1}^n |y_i - \hat{y}_i|, \quad (19)$$

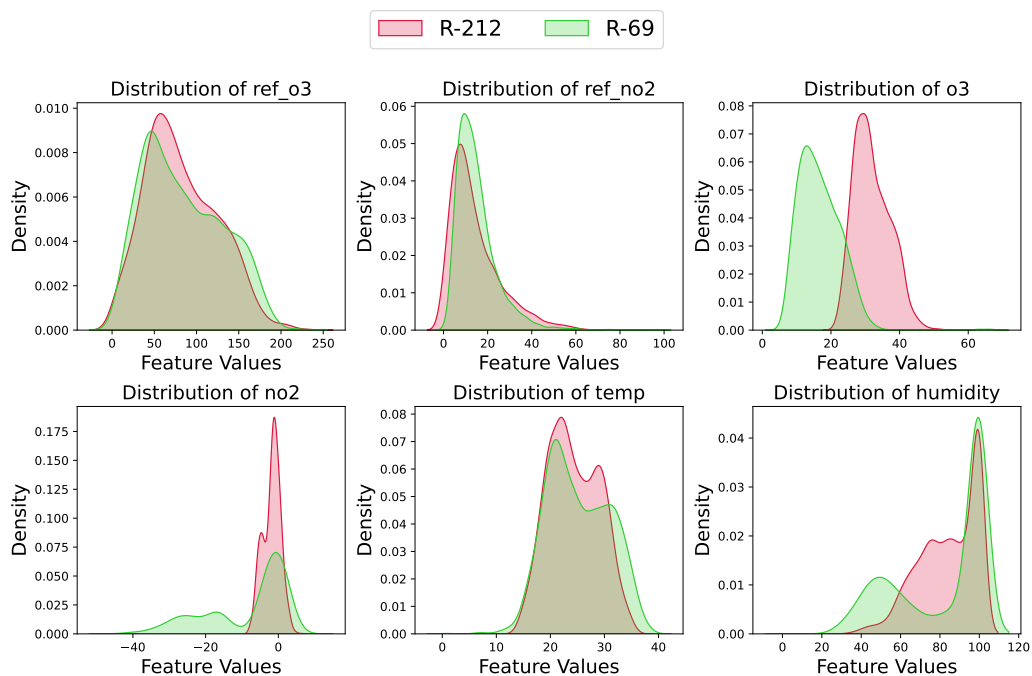


Figure 5: Distribution of features and labels between two datasets using Kernel Density Estimation (KDE) plots.

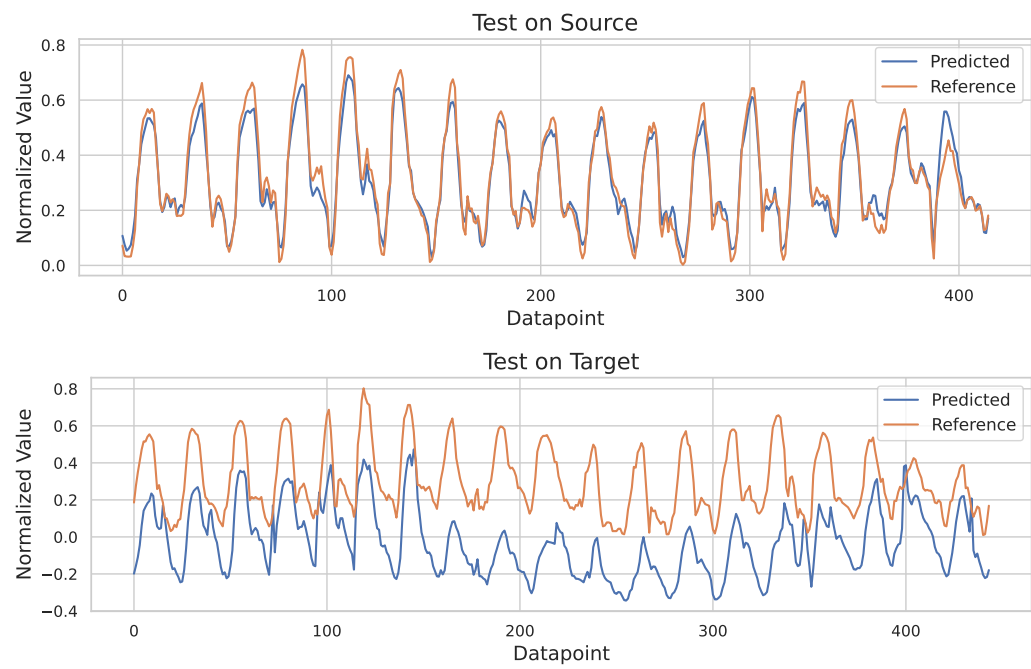


Figure 6: Impact of distribution shift between source and target data in different measurement locations on the model performance.

In these equations,  $n$  represents the total number of samples,  $y_i$  is the actual observed value for the  $i$ -th estimation, and  $\hat{y}_i$  is the predicted value for the  $i$ -th estimation. To provide a more comprehensive analysis, we evaluate the methods using both normalized and unnormalized labels. Normalized labels allow for results to be compared on a common scale, which is particularly useful when working with diverse datasets. Conversely, unnormalized labels retain the original scale of the data, providing insights into real-world applications.

#### 4.4. Comparison Methods

In this subsection, we present a comparative analysis of our proposed TikUDA algorithm against various UDA methods that address the challenges posed by distribution shifts between source and target domains. Each method employs a unique strategy to mitigate these distribution shifts, providing a thorough and comprehensive comparison.

The following methods are considered for the comparison:

- **Source-Only:** A baseline method where a model is trained exclusively on the source domain data and then directly applied to the target domain data. This approach does not involve any domain adaptation techniques, potentially leading to degraded performance when there is a distribution shift between the source and target domains. This approach usually serves as the lower bound of the performance.
- **Maximum Mean Discrepancy (MMD):** A distance-based domain adaptation method that assesses the difference between two empirical probability distributions [24]. It embeds the distributions in a reproducing kernel Hilbert space to measure the distance between them.
- **Adaptive Batch Normalization (AdaBN):** AdaBN [41] is a domain adaptation method that adjusts the batch normalization parameters of a trained model based on the target domain data. Unlike other methods that focus on learning domain-invariant features, AdaBN modifies the batch normalization statistics to fit the target domain. The model parameters are trained solely on the source domain data, with target domain data used only to update the normalization statistics. This requires the feature extractor to include batch normalization layers to implement AdaBN.

- **Correlation Alignment (CORAL):** CORAL [42] aligns the second-order statistics (mean and covariance) of the source and target domain features. This method distinguishes itself from subspace manifold approaches by aligning the original feature distributions of the source and target domains, rather than focusing on the bases of lower-dimensional subspaces.
- **Empirical Risk Minimization with Nuclear Norm Regularization (ERM-NU):** ERM-NU [43] combines empirical risk minimization with nuclear norm regularization. This method addresses low-rank matrix completion and recovery problems using nuclear norm minimization. ERM-NU aims to obtain domain-invariant features. By minimizing the nuclear norm of the features, ERM-NU seeks to reduce the rank and thus enhance the alignment between domains.
- **Aligning the Inverse GRAM Matrices (DARE-GRAM):** DARE-GRAM aligns the inverse GRAM matrices of the source and target domains to mitigate distribution shifts. This alignment strategy aims to improve model performance on the target domain by reducing discrepancies between the domain distributions.

#### 4.5. Implementation Details

In this study, all compared methods share the same base architecture, except for AdaBN, which includes an additional batch normalization layer after the GAT layer to ensure a fair comparison. To determine the number of layers and the hidden dimension of the feature extractor, we split the source domain dataset into training and testing sets to perform model selection based on the labeled source data. This approach ensures that the feature extractor can effectively extract the necessary informative features for multisensor fusion and calibration tasks.

The feature extractor consists of four GRU layers and one GAT layer, with all layers (linear encoder, GRU, and GAT) set to a hidden dimension of 16. The remaining architecture includes a regressor, comprising one fully connected layer to predict the final output value. The model is updated using the Adam optimizer [44] with a learning rate of  $3 \times 10^{-4}$  and batch sizes of 64, over 150 epochs. For each training step, one batch of source and target domain data is processed.

Due to the absence of a labeled validation dataset, the hyperparameters and training specifications mentioned above were primarily chosen based on

prior work [45]. In our approach, the hyperparameters  $\gamma_{\text{angle}}$  and  $\gamma_{\text{scale}}$ , as defined in equation (17), were set to  $\gamma_{\text{angle}} = 10^{-2}\lambda$  and  $\gamma_{\text{scale}} = 10^{-3}\lambda$ , respectively for ‘R-212 to R-69 ( $O_3$ )’ scenario. Here,  $\lambda = \frac{2}{1+\exp(-10p)} - 1$  and  $p$  represents the progress of training iterations, allowing  $\lambda$  to range from 0 to 1. Consequently,  $\gamma_{\text{angle}}$  and  $\gamma_{\text{scale}}$  vary from 0 to  $10^{-2}$  and  $10^{-3}$ , respectively. This follows a similar approach to [46, 47].

## 5. Results and Discussion

Table 2: RMSE Results for Four Domain Adaptation Scenarios

Scenario	R-212 → R-69 ( $O_3$ )		R-212 → R-69 ( $NO_2$ )		R-69 → R-212 ( $O_3$ )		R-69 → R-212 ( $NO_2$ )		Avg.
Method	Norm. ↓	Actual ↓	Norm. ↓	Actual ↓	Norm. ↓	Actual ↓	Norm. ↓	Actual ↓	Norm. ↓
Source-Only	0.255	59.40	0.183	11.88	0.217	48.44	0.117	11.11	0.193
MMD [24]	0.159	37.13	0.139	9.03	0.118	26.25	0.105	9.99	0.130
AdaBN [41]	0.254	59.39	0.289	18.67	0.118	26.29	0.106	10.05	0.192
CORAL [42]	0.205	47.71	0.158	10.27	0.175	39.03	0.104	9.89	0.161
ERM-NU [43]	0.184	43.19	0.146	9.48	0.124	27.62	0.102	9.67	0.139
DARE-GRAM [30]	<u>0.094</u>	<u>22.01</u>	<b>0.133</b>	<b>8.60</b>	<u>0.102</u>	<u>22.37</u>	<b>0.098</b>	<b>9.35</b>	<u>0.107</u>
TikUDA	<b>0.087</b>	<b>20.35</b>	<u>0.137</u>	<u>8.88</u>	<u>0.097</u>	<b>21.87</b>	<u>0.099</u>	<u>9.37</u>	<b>0.105</b>

Table 3: MAE Results for Four Domain Adaptation Scenarios

Scenario	R-212 → R-69 ( $O_3$ )		R-212 → R-69 ( $NO_2$ )		R-69 → R-212 ( $O_3$ )		R-69 → R-212 ( $NO_2$ )		Avg.
Method	Norm. ↓	Actual ↓	Norm. ↓	Actual ↓	Norm. ↓	Actual ↓	Norm. ↓	Actual ↓	Norm. ↓
Source-Only	0.221	51.47	0.135	8.69	0.194	43.35	0.092	8.79	0.161
MMD [24]	0.129	30.21	0.097	6.30	0.090	20.16	0.080	7.62	0.099
AdaBN [41]	0.209	48.95	0.241	15.60	0.094	20.93	0.082	7.76	0.157
CORAL [42]	0.168	39.28	0.115	7.41	0.148	32.95	0.079	7.51	0.128
ERM-NU [43]	0.159	37.29	0.112	7.25	0.099	22.04	<u>0.073</u>	<u>6.92</u>	0.111
DARE-GRAM [30]	<u>0.077</u>	<u>17.83</u>	<u>0.095</u>	<u>6.11</u>	<u>0.081</u>	<u>17.66</u>	<u>0.073</u>	<u>6.94</u>	<u>0.082</u>
TikUDA	<b>0.070</b>	<b>16.38</b>	<u>0.093</u>	<b>6.02</b>	<u>0.076</u>	<b>17.17</b>	<u>0.072</u>	<b>6.79</b>	<b>0.078</b>

In this section, we assess the effectiveness of all compared methods based on their performance using RMSE and MAE metrics, as shown in Tables 2 and 3, respectively. The source-only model reveals that the prediction error for the  $O_3$  is more than four times larger than for the  $NO_2$  task in both transfer scenarios, indicating a significant domain shift in  $O_3$  estimation. Specifically, for the  $O_3$  task, our proposed method significantly improves RMSE from 59.40 (source-only model) to 20.35 (TikUDA) for the transfer task ‘R-212 to R-69’, and from 48.44 (source-only model) to 21.87 (TikUDA) for the transfer task ‘R-69 to R-212’. Overall, TikUDA demonstrates the best average performance compared to other methods across all adaptation

and transfer scenarios, achieving an average RMSE of 0.105 and an average MAE of 0.078, outperforming all other methods.

DARE-GRAM shows the second-best performance with an average RMSE of 0.107 and an average MAE of 0.082, indicating that the proposed haversine distance function effectively helps align the source and target domains. Additionally, the proposed approximation of the Gram matrix using TikUDA did not negatively impact performance. Other methods such as MMD, CORAL, and ERM-NU also showed improvements in RMSE and MAE compared to the baseline, as indicated in Tables 2 and 3. However, they did not achieve the same level of performance, as they are not primarily designed for regression tasks like DARE-GRAM and TikUDA.

Additionally, we evaluate the impact of our approach on the embeddings generated during the alignment process for the adaptation scenario of R-212  $\rightarrow$  R-69 ( $O_3$ ). We applied principal component analysis (PCA) to the embedded features and plotted the first two principal components to create two-dimensional visualizations, as depicted in Figure 7. The PCA plot highlights a significant discrepancy between the source and target data distributions when using the source-only model. In contrast, our proposed method achieves a better alignment of data points from both domains, demonstrating its effectiveness in mitigating distribution shifts in the feature space.

Furthermore, we compare the time complexity of our proposed algorithm with DARE-GRAM, as these two algorithms performed best in our experiments and share similar theoretical underpinnings, warranting a focused analysis. In other words, since these two methods are subspace-based approaches specifically designed for regression tasks, it is appropriate to present their running times side by side for a direct comparison. Both DARE-GRAM and TikUDA exhibit similar asymptotic computational complexities, approximately  $\mathcal{O}(p^3)$ , but differ significantly in their practical execution. DARE-GRAM relies on full SVD and the computation of the Moore-Penrose pseudo-inverse, which leads to higher computational overhead. Specifically, calculating the Gram matrix for both methods requires  $\mathcal{O}(bp^2)$ , where  $b$  is the batch size and  $p$  is the feature dimension. The SVD step further introduces an  $\mathcal{O}(p^3)$  complexity, and computing the pseudo-inverse also contributes an additional  $\mathcal{O}(p^3)$ , making DARE-GRAM computationally expensive. In contrast, TikUDA utilizes power iteration to approximate the largest singular value, avoiding the need for full SVD. Each iteration of the power method takes  $\mathcal{O}(p^2)$ . Moreover, TikUDA leverages Cholesky decomposition, which has a complexity of  $\mathcal{O}(p^3/3)$ , for matrix inversion, offering a more efficient

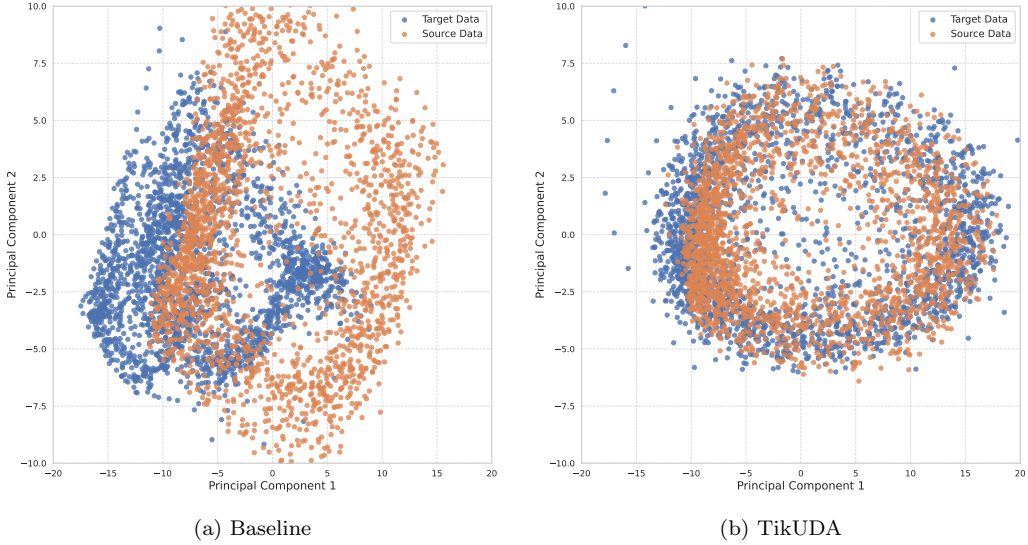


Figure 7: Visualization of the impact of the feature alignment with the proposed method on the (R-212 → R-69 (O<sub>3</sub>)) task

alternative to SVD-based inversion. While both methods have similar theoretical upper bounds, the use of power iteration and Cholesky decomposition in TikUDA significantly reduce the constant factor in the complexity, leading to faster performance in practice compared to DARE-GRAM. Consequently, TikUDA is expected to perform more efficiently, especially for large-scale data, where full SVD can be prohibitively slow.

For comparing practical time complexity, Figure 8 illustrates the comparison of running times between DARE-GRAM and TikUDA across different sizes of hidden dimensions during each training iteration conducted on NVIDIA GeForce RTX 2080 Ti GPU. As the hidden dimensions increase, the computation time for DARE-GRAM escalates significantly, whereas TikUDA maintains a much faster performance in high-dimensional settings. This efficiency is particularly beneficial for graph-structured data, where the number of nodes and hidden dimensions can be substantial.

### 5.1. Ablation Studies

In this subsection, we explore the effects of aligning angles and scaling eigenvalues on model performance through ablation studies. We select the tasks R-212 → R-69 (O<sub>3</sub>) and R-69 → R-212 (O<sub>3</sub>) for this analysis. As illustrated in Table 4, aligning both angles and scales in the proposed method

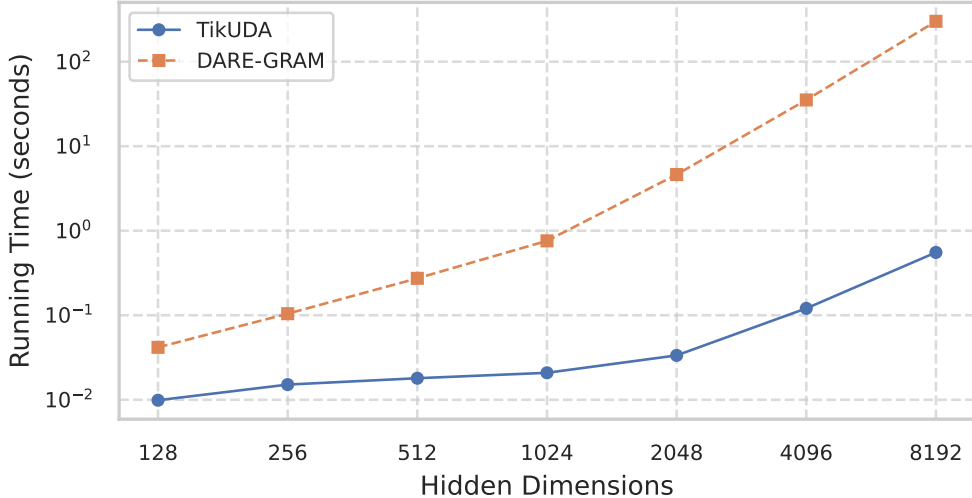


Figure 8: Comparison of running times on training iteration for TikUDA and DARE-GRAM across varying hidden dimensions (128 to 8192).

Table 4: RMSE ( $\downarrow$ ) Values for Ablation Studies

Method	R-212 $\rightarrow$ R-69 ( $O_3$ )	R-69 $\rightarrow$ R-212 ( $O_3$ )
Source-Only	0.255	0.217
$\gamma_{\text{angle}} = 0$	0.096	0.106
$\gamma_{\text{scale}} = 0$	0.202	0.159
<b>Both (TikUDA)</b>	<b>0.087</b>	<b>0.099</b>

results in performance enhancements compared to the source-only approach. Notably, scaling alignment significantly reduces the RMSE compared to the source-only baseline by ensuring the range of predicted values aligns across different datasets. Meanwhile, aligning angles alone yields a smaller improvement in performance.

The Tikhonov matrix introduces the hyperparameter  $\alpha$ . If  $\alpha$  is too low, the matrix may not be fully ranked, leading to numerical instability. Conversely, a large  $\alpha$  can cause the identity matrix subspace to become more prominent than that of the Gram matrix, which is undesirable for alignment. Our analysis of the R-212  $\rightarrow$  R-69 ( $O_3$ ) case, illustrated in Figure 9, shows that our method is relatively insensitive to variations in  $\alpha$ . This indicates that the specific choice of  $\alpha$  is not critical to the performance of

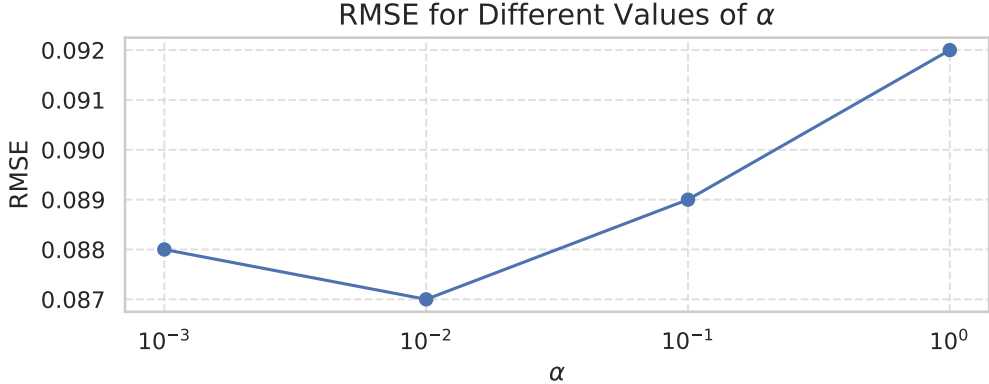


Figure 9: Impact of Different Values of  $\alpha$  on RMSE

our proposed method.

## 6. Conclusion

This paper investigates the challenge of unsupervised domain adaptation regression within spatial-temporal graph neural networks, specifically focusing on the fusion and calibration of multisensor data in IoT air quality sensor networks. Our approach addresses domain adaptation for regression tasks by integrating the Tikhonov-regularized closed-form least square solution. Additionally, we introduce a novel method for scaling and aligning the Tikhonov matrix, which reduces complexity and improves accuracy. Experimental results demonstrate substantial improvements in the model’s generalization ability across four different real-world scenarios. The findings of this paper open up several potential directions for future research. Firstly, TikUDA is a model-agnostic method, indicating its applicability to various datasets and tasks across different fields, including computer vision, and multimodal learning. Moreover, future work can focus on exploring alternative regularization techniques, beyond ridge regression, that offer closed-form solutions for inverse problems. Implementing these techniques in unsupervised domain adaptation tasks holds promise for further advancements in the field.

## Appendix A. Details on Power Method

The power iteration method is a widely used algorithm for finding the largest eigenvalue and its corresponding eigenvector of a matrix. It is particularly efficient for large matrices where computing the full spectrum of eigenvalues and eigenvectors (such as methods like SVD) would be computationally expensive. Power iteration approximates only the largest eigenvalue, making it suitable for tasks requiring less detailed spectral information. The algorithm begins by randomly initializing a vector  $\mathbf{v}_0 \in \mathbb{R}^p$ . In each iteration, the vector is updated by multiplying it by the matrix  $\mathbf{A}$ , normalizing it to prevent it from growing unbounded. Specifically, for each iteration  $k$ , the new vector  $\mathbf{v}_k$  is computed as:

$$\mathbf{v}_k = \frac{\mathbf{A}\mathbf{v}_{k-1}}{\|\mathbf{A}\mathbf{v}_{k-1}\|}, \quad (\text{A.1})$$

where  $\|\cdot\|$  represents the norm. Over several iterations, the vector  $\mathbf{v}_k$  converges to the eigenvector associated with the largest eigenvalue  $\lambda_{\max}$ . Once the algorithm converges, the largest eigenvalue can be approximated by:

$$\lambda_{\max} \approx \frac{\mathbf{v}_k^\top \mathbf{A} \mathbf{v}_k}{\mathbf{v}_k^\top \mathbf{v}_k}. \quad (\text{A.2})$$

## Appendix B. Generalization to Other Applications

**Electroencephalography (EEG) Dataset:** EEG signals are widely used in neuroscience and biomedical research due to their ability to capture the brain’s electrical activity in a non-invasive manner. The primary motivation for selecting an EEG dataset for this study lies in its inherent complexity, with significant variations in brain activity both within and across subjects. This complexity creates a challenging yet realistic setting for evaluating domain adaptation techniques. Due to the natural inter-subject variability in EEG signals, they serve as an ideal benchmark for evaluating our proposed TikUDA method. Effective knowledge transfer across domains, specifically between different subjects – is essential in applications such as brain-computer interfaces (BCIs) and neurological disorder diagnostics, where models must generalize across individuals with unique brainwave patterns.

The EEG recordings were obtained using a Neurocom 23-channel EEG system (Ukraine, XAI-MEDICA) configured in a monopolar setup [48]. Silver/silver chloride electrodes were positioned on the scalp following the International 10/20 system, with all electrodes referenced to interconnected ear reference electrodes. The data were processed using a high-pass filter with a 30 Hz cutoff and a 50 Hz power line notch filter. Artifact-free EEG segments, each lasting 60 seconds, were selected for analysis. During preprocessing, Independent Component Analysis (ICA) was employed to remove artifacts caused by eye movements, muscle activity, and cardiac pulsations. Participants engaged in a cognitive task involving the serial subtraction of two numbers, where each trial began with the oral presentation of a 4-digit minuend and a 2-digit subtrahend. The channels selected for analysis included Fp1, Fp2, F3, F4, F7, F8, T3, T4, C3, C4, T5, T6, P3, P4, O1, O2, Fz, Cz, and Pz as illustrated in Fig. B.10

For the regression task, we focused on reconstructing the missing FP1 channel using the remaining active channels. In the domain adaptation task, we selected two subjects: Subject 00, a 21-year-old female, and Subject 33, a 17-year-old male. We assume that FP1 measurements are available for Subject 33, but for Subject 00, due to technical issues with the EEG cap, the FP1 channel was not recorded properly. This simulates a real-world scenario where sensor (electrode) malfunction or noise leads to missing data, and the goal is to leverage the data from other channels and the source subject (Subject 33) to accurately reconstruct the missing measurements for the target subject (Subject 00). This setting allows us to test the robustness of our method in handling missing data and domain shifts simultaneously.

We compared the same methods used in the air quality task and the STGNN architecture remained unchanged, allowing for a direct comparison of the approaches. The results in Table B.5 highlight that in the domain adaptation scenario ( $S_{33} \rightarrow S_{00}$ ) for EEG signals, while several methods perform well. However, TikUDA is consistently the best performing method. Specifically, while MMD and ERM-NU achieve competitive performance – with ERM-NU achieving an RMSE of 0.180 and an MAE of 0.132 – TikUDA outperforms these methods, achieving the lowest RMSE of 0.178 and the lowest MAE of 0.130. These findings demonstrate the effectiveness and robustness of TiKUDA in enhancing prediction accuracy for EEG-based domain adaptation tasks. Moreover, they confirm TiKUDA’s broad applicability to other UDA regression tasks across various domains.

**Details on Hyperparameters Tuning:** In UDA, the absence of labeled

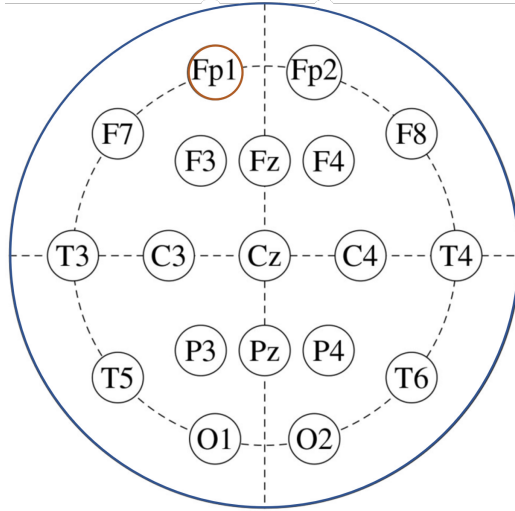


Figure B.10: EEG setup with 19 channels.

Table B.5: Results for Domain Adaptation Scenario (S33  $\rightarrow$  S00) on EEG Signals

Method	RMSE (Norm.) $\downarrow$	RMSE (Actual) $\downarrow$	MAE (Norm.) $\downarrow$	MAE (Actual) $\downarrow$
Source-Only	0.327	21.96	0.253	17.01
MMD	0.182	12.24	0.134	8.99
AdaBN	0.294	19.78	0.225	15.18
CORAL	0.318	21.44	0.246	16.59
ERM-NU	<u>0.180</u>	<u>12.12</u>	<u>0.132</u>	<u>8.86</u>
DARE-GRAM	0.205	13.82	0.154	10.40
TikUDA	<b>0.178</b>	<b>12.03</b>	<b>0.130</b>	<b>8.76</b>

data for the target domain makes it impossible to utilize a validation dataset for hyperparameter tuning. Consequently, an alternative approach must be adopted. We employed a heuristic method proposed in [45], which addresses this challenge.

Our observations indicated that if the trade-off alignment regularization is set too high for all methods, it hinders the model’s ability to learn effectively. Conversely, if it is too low, there is insufficient adaptation to the target domain. To tune the hyperparameters, we conducted a search over specific values and tracked the normalized summation of the source loss and the trade-off alignment loss. This process was applied to all methods to ensure a fair comparison.

Table B.6 summarizes the search space and the selected hyperparameters for each method, with the chosen hyperparameters indicated in bold.

Table B.6: Hyperparameters Used for UDA in Our Experiments on EEG Data

Method	Hyperparameters
MMD [24]	Tradeoff alignment loss: {0.25, 0.025, <b>0.0025</b> }
CORAL [42]	Tradeoff alignment loss: { <b>0.25</b> , 0.025, 0.0025}
ERM-NU [43]	Tradeoff alignment loss: {0.25, <b>0.025</b> , 0.0025}
DARE-GRAM [30]	Tradeoff angle alignment loss: {0.5, <b>0.05</b> , 0.005} Tradeoff scale alignment loss: {0.25, <b>0.025</b> , 0.0025}
TikUDA	Tradeoff angle alignment loss: {0.5, <b>0.05</b> , 0.005} Tradeoff scale alignment loss: {0.25, <b>0.025</b> , 0.0025}

## Acknowledgement

This research was supported by the Swiss Federal Institute of Metrology (METAS).

## References

- [1] X. Lu, L. Zhang, L. Shen, Meteorology and climate influences on tropospheric ozone: a review of natural sources, chemistry, and transport patterns, *Current Pollution Reports* 5 (2019) 238–260.
- [2] S. E. Bibri, J. Krogstie, A. Kaboli, A. Alahi, Smarter eco-cities and their leading-edge artificial intelligence of things solutions for environmental sustainability: A comprehensive systematic review, *Environmental Science and Ecotechnology* 19 (2024) 100330.
- [3] B. P. L. Lau, S. H. Marakkalage, Y. Zhou, N. U. Hassan, C. Yuen, M. Zhang, U.-X. Tan, A survey of data fusion in smart city applications, *Information Fusion* 52 (2019) 357–374.
- [4] S. E. Bibri, A. Alahi, A. Sharifi, J. Krogstie, Environmentally sustainable smart cities and their converging ai, iot, and big data technologies and solutions: an integrated approach to an extensive literature review, *Energy Informatics* 6 (2023) 9.
- [5] A. Lewis, W. R. Peltier, E. von Schneidemesser, Low-cost sensors for the measurement of atmospheric composition: overview of topic and future applications (2018).

- [6] B. P. L. Lau, N. Wijerathne, B. K. K. Ng, C. Yuen, Sensor fusion for public space utilization monitoring in a smart city, *IEEE Internet of Things Journal* 5 (2017) 473–481.
- [7] P. Ferrer-Cid, J. M. Barcelo-Ordinas, J. Garcia-Vidal, A. Ripoll, M. Viana, Multisensor data fusion calibration in iot air pollution platforms, *IEEE Internet of Things Journal* 7 (2020) 3124–3132.
- [8] E. S. Cross, L. R. Williams, D. K. Lewis, G. R. Magoon, T. B. Onasch, M. L. Kaminsky, D. R. Worsnop, J. T. Jayne, Use of electrochemical sensors for measurement of air pollution: correcting interference response and validating measurements, *Atmospheric Measurement Techniques* 10 (2017) 3575–3588.
- [9] M. R. Giordano, C. Malings, S. N. Pandis, A. A. Presto, V. McNeill, D. M. Westervelt, M. Beekmann, R. Subramanian, From low-cost sensors to high-quality data: A summary of challenges and best practices for effectively calibrating low-cost particulate matter mass sensors, *Journal of Aerosol Science* 158 (2021) 105833.
- [10] P. Ferrer-Cid, J. A. Paredes-Ahumada, X. Allka, M. Guerrero-Zapata, J. M. Barcelo-Ordinas, J. Garcia-Vidal, A data-driven framework for air quality sensor networks, *IEEE Internet of Things Magazine* 7 (2024) 128–134.
- [11] X. Allka, P. Ferrer-Cid, J. M. Barcelo-Ordinas, J. Garcia-Vidal, Temporal pattern-based denoising and calibration for low-cost sensors in iot monitoring platforms, *IEEE Transactions on Instrumentation and Measurement* 72 (2023) 1–11. [10.1109/TIM.2023.3239626](https://doi.org/10.1109/TIM.2023.3239626).
- [12] G. Jin, Y. Liang, Y. Fang, Z. Shao, J. Huang, J. Zhang, Y. Zheng, Spatio-temporal graph neural networks for predictive learning in urban computing: A survey, *IEEE Transactions on Knowledge and Data Engineering* (2023).
- [13] Z. Cui, K. Henrickson, R. Ke, Y. Wang, Traffic graph convolutional recurrent neural network: A deep learning framework for network-scale traffic learning and forecasting, *IEEE Transactions on Intelligent Transportation Systems* 21 (2020) 4883–4894.

- [14] W. Jiang, J. Luo, Graph neural network for traffic forecasting: A survey, *Expert Systems with Applications* (2022) 117921.
- [15] K.-H. N. Bui, J. Cho, H. Yi, Spatial-temporal graph neural network for traffic forecasting: An overview and open research issues, *Applied Intelligence* 52 (2022) 2763–2774.
- [16] K. F. Niresi, H. Bissig, H. Baumann, O. Fink, Physics-enhanced graph neural networks for soft sensing in industrial internet of things, 2024. [arXiv:2404.08061](https://arxiv.org/abs/2404.08061).
- [17] M. Zhao, O. Fink, Dyedgegat: Dynamic edge via graph attention for early fault detection in iiot systems, *IEEE Internet of Things Journal* (2024).
- [18] S. Min, Z. Gao, J. Peng, L. Wang, K. Qin, B. Fang, Stgsn—a spatial-temporal graph neural network framework for time-evolving social networks, *Knowledge-Based Systems* 214 (2021) 106746.
- [19] K. F. Niresi, M. Zhao, H. Bissig, H. Baumann, O. Fink, Spatial-temporal graph attention fuser for calibration in iot air pollution monitoring systems, in: 2023 IEEE SENSORS, IEEE, 2023, pp. 01–04.
- [20] S. Ben-David, J. Blitzer, K. Crammer, F. Pereira, Analysis of representations for domain adaptation, *Advances in neural information processing systems* 19 (2006).
- [21] G. Wilson, D. J. Cook, A survey of unsupervised deep domain adaptation, *ACM Transactions on Intelligent Systems and Technology (TIST)* 11 (2020) 1–46.
- [22] R. Cai, J. Chen, Z. Li, W. Chen, K. Zhang, J. Ye, Z. Li, X. Yang, Z. Zhang, Time series domain adaptation via sparse associative structure alignment, in: *Proceedings of the AAAI Conference on Artificial Intelligence*, volume 35, 2021, pp. 6859–6867.
- [23] Q. Liu, H. Xue, Adversarial spectral kernel matching for unsupervised time series domain adaptation., in: *IJCAI*, 2021, pp. 2744–2750.
- [24] M. Long, Y. Cao, J. Wang, M. Jordan, Learning transferable features with deep adaptation networks, in: *International conference on machine learning*, PMLR, 2015, pp. 97–105.

- [25] X. Shen, Q. Dai, F.-l. Chung, W. Lu, K.-S. Choi, Adversarial deep network embedding for cross-network node classification, in: Proceedings of the AAAI conference on artificial intelligence, volume 34, 2020, pp. 2991–2999.
- [26] X. Ma, T. Zhang, C. Xu, Gcan: Graph convolutional adversarial network for unsupervised domain adaptation, in: Proceedings of the IEEE/CVF Conference on Computer Vision and Pattern Recognition, 2019, pp. 8266–8276.
- [27] R. Zhu, X. Jiang, J. Lu, S. Li, Cross-domain graph convolutions for adversarial unsupervised domain adaptation, *IEEE Transactions on Neural Networks and Learning Systems* (2021).
- [28] Y. Ganin, E. Ustinova, H. Ajakan, P. Germain, H. Larochelle, F. Laviolette, M. March, V. Lempitsky, Domain-adversarial training of neural networks, *Journal of machine learning research* 17 (2016) 1–35.
- [29] X. Chen, S. Wang, J. Wang, M. Long, Representation subspace distance for domain adaptation regression., in: ICML, 2021, pp. 1749–1759.
- [30] I. Nejjar, Q. Wang, O. Fink, DARE-GRAM: unsupervised domain adaptation regression by aligning inverse gram matrices, in: Proceedings of the IEEE/CVF Conference on Computer Vision and Pattern Recognition, 2023, pp. 11744–11754.
- [31] G. Jin, Y. Liang, Y. Fang, Z. Shao, J. Huang, J. Zhang, Y. Zheng, Spatio-temporal graph neural networks for predictive learning in urban computing: A survey, 2023. [arXiv:2303.14483](https://arxiv.org/abs/2303.14483).
- [32] S. P. Boyd, L. Vandenberghe, Convex optimization, Cambridge university press, 2004.
- [33] C. Lanczos, An iteration method for the solution of the eigenvalue problem of linear differential and integral operators (1950).
- [34] M. Jin, H. Y. Koh, Q. Wen, D. Zambon, C. Alippi, G. I. Webb, I. King, S. Pan, A survey on graph neural networks for time series: Forecasting, classification, imputation, and anomaly detection, *arXiv preprint arXiv:2307.03759* (2023).

- [35] K. Xu, W. Hu, J. Leskovec, S. Jegelka, How powerful are graph neural networks?, in: International Conference on Learning Representations, 2019.
- [36] J. Gao, B. Ribeiro, On the equivalence between temporal and static equivariant graph representations, in: International Conference on Machine Learning, PMLR, 2022, pp. 7052–7076.
- [37] W. L. Hamilton, Graph representation learning, Morgan & Claypool Publishers, 2020.
- [38] P. Veličković, G. Cucurull, A. Casanova, A. Romero, P. Liò, Y. Bengio, Graph attention networks, in: International Conference on Learning Representations, 2018.
- [39] A. Ripoll, M. Viana, M. Padrosa, X. Querol, A. Minutolo, K. M. Hou, J. M. Barcelo-Ordinas, J. García-Vidal, Testing the performance of sensors for ozone pollution monitoring in a citizen science approach, *Science of the total environment* 651 (2019) 1166–1179.
- [40] J. M. Barcelo-Ordinas, P. Ferrer-Cid, J. Garcia-Vidal, M. Viana, A. Ripoll, H2020 project captor dataset: Raw data collected by low-cost mox ozone sensors in a real air pollution monitoring network, *Data in brief* 36 (2021) 107127.
- [41] Y. Li, N. Wang, J. Shi, X. Hou, J. Liu, Adaptive batch normalization for practical domain adaptation, *Pattern Recognition* 80 (2018) 109–117.
- [42] B. Sun, K. Saenko, Deep coral: Correlation alignment for deep domain adaptation, in: Computer Vision–ECCV 2016 Workshops: Amsterdam, The Netherlands, October 8–10 and 15–16, 2016, Proceedings, Part III 14, Springer, 2016, pp. 443–450.
- [43] Z. Shi, Y. Ming, Y. Fan, F. Sala, Y. Liang, Domain generalization via nuclear norm regularization, in: Conference on Parsimony and Learning, PMLR, 2024, pp. 179–201.
- [44] D. P. Kingma, J. Ba, Adam: A method for stochastic optimization, in: International Conference on Learning Representations (ICLR), 2015, pp. 1–15.

- [45] Y. Sun, E. Tzeng, T. Darrell, A. A. Efros, Unsupervised domain adaptation through self-supervision, arXiv preprint arXiv:1909.11825 (2019).
- [46] Y. Ganin, V. Lempitsky, Unsupervised domain adaptation by backpropagation, in: International conference on machine learning, PMLR, 2015, pp. 1180–1189.
- [47] I. Nejjar, G. Frusque, F. Forest, O. Fink, Uncertainty-guided alignment for unsupervised domain adaptation in regression, arXiv preprint arXiv:2401.13721 (2024).
- [48] I. Zyma, S. Tukaev, I. Seleznov, K. Kiyono, A. Popov, M. Chernykh, O. Shpenkov, Electroencephalograms during mental arithmetic task performance, Data 4 (2019) 14.